**Acoustically driven photon anti-bunching in nanowires**

A. Hernández-Mínguez, M.Möller, S. Breuer, C. Pfüller, C. Somaschini, S. Lazić, O. Brandt, A. García-Cristóbal, M. M. de Lima, Jr., A. Cantarero, L. Geelhaar, H. Riechert, and P. V. Santos

This supplementary information contains:

## A. Amplitude of the piezoelectric field

The acoustic transport experiments were carried out on delay lines fabricated on 128° Y-cut $LiNbO_3$ wafers. The delay line employs floating electrode unidirectional transducers[1] (IDTs) designed to generate multiple harmonics of the fundamental wavelength $\lambda_{SAW0} = 35\ \mu$m. The experiments reported on the paper were carried out using the second and third harmonics with $\lambda_{SAW} = 17.5\ \mu$m and 11.67 $\mu$m, respectively, as they are the ones showing the highest electro-acoustic conversion efficiency. For both harmonics, the acoustic wavelength is much larger than the acoustic transport distances. They correspond to resonance bands centered at frequencies of 220 and 330 MHz at room temperature, whereas at 20 K they appear at 226 and 338 MHz, respectively. The IDTs are 700 $\mu$m long and have an aperture (approximately equal to the finger length) of $l_{IDT} = 400\ \mu$m. The $s_{11}$ rf power reflection parameter for these transducers and the $s_{21}$ rf power transmission for the delay line around the resonance of the $\lambda_{SAW} = 17.5\ \mu$m mode are shown in Figs. S1a and S1b. These measurements were carried out at room temperature using an rf connection configuration similar to the one for the low temperature measurements. The IDTs have a 3.5 MHz wide emission band, as defined by the frequency range, where the transmission is within 3 dB of its maximum value. The insertion loss of the delay line is 10.6 dB at the resonance frequency of 226 MHz.

Since the delay line is symmetric (i.e., with equal IDTs), the electro-acoustic conversion efficiency is simply half of the insertion loss in dB determined from the $s_{12}$ transmission spectra (i.e., 5.3 dB). The IDTs convert, therefore, $r_a = 29.5\%$ of the input electrical power applied to the IDT into acoustic power.

## B. Dependence of the transfer efficiency on rf frequency and power

The experiments described in the main paper were carried out by exciting the IDTs at the center of their resonance band. In order to show that transport along the nanowire (NW) only takes place within this frequency range we plot in Fig. S1c the relative photon transfer efficiency for sample A defined by

$$r_t = \frac{I_{PL}(x_r)}{I_{PL}(0) + I_{PL}(x_r)}, \tag{S1}$$

where $I_{PL}(x)$ denotes the photoluminescence (PL) intensity emitted at location $x$ and $x_r$ is the coordinate of the remote emission point. $r_t$ is characterized by a maximum centered at 225 MHz induced by the acoustic transport of charge, which corresponds to the acoustic emission band of the IDT at 20 K (we verified that the latter is $\Delta f_{\mathrm{SAW}} = 3$ MHz higher than at room temperature). Note that $r_t$ has significant values only within the SAW emission range: the residual background outside this range is attributed to carrier diffusion to the remote trap.

Figure 2 of the main text shows that acoustic transport takes place over a wide range of

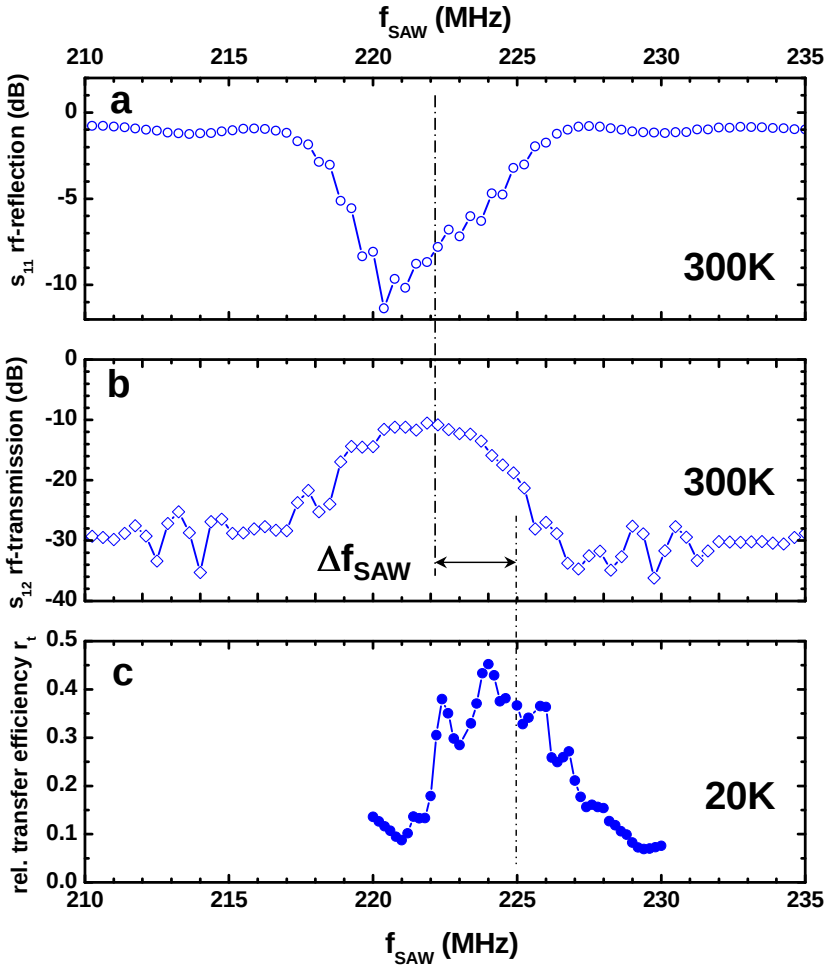


FIG. S1. **Correlation between surface acoustic wave (SAW) excitation and acoustic transport.** **a,** $s_{11}$ rf power reflection coefficient **b,** $s_{21}$ rf power transmission coefficient of the SAW delay line used in the acoustic transport experiments measured at room temperature. **c,** Frequency dependence of the transfer efficiency $r_t$ carried out using a fixed rf power of 11 dBm. The frequency shift $\Delta f_{\mathrm{SAW}}$ is due to the different measurement temperatures.

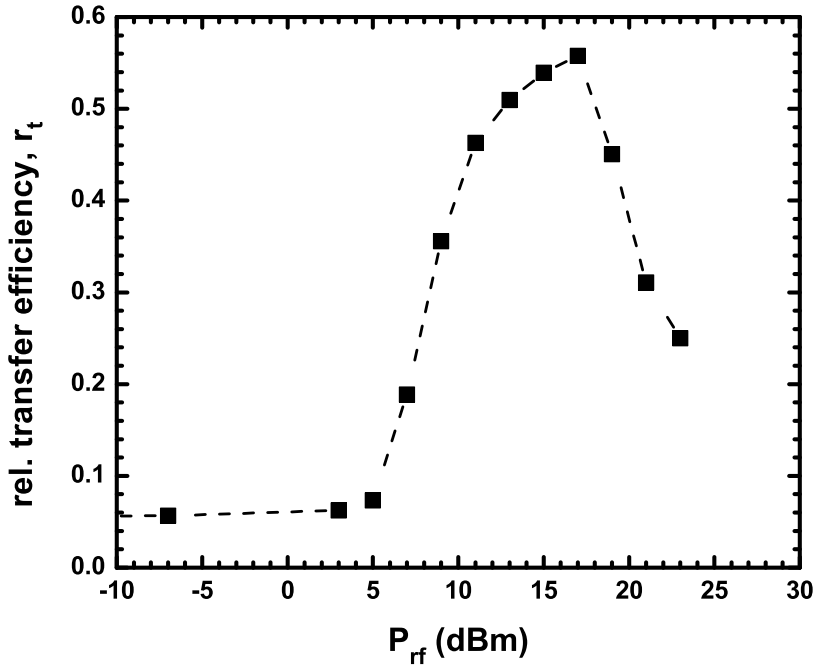


FIG. S2. **Dependence of the transfer efficiency $r_t$ for sample A on the rf power applied to the transducer**. The experiment was carried out at a fixed rf frequency of 226.5 MHz. The solid line is a guide to the eye.

acoustic powers. Figure S2 displays the dependence of the transfer efficiency $r_t$ on acoustic power. The onset of transport occurs at $P_{\rm rf} \approx 3$ dBm, which corresponds to an acoustic linear power density $P_{\rm SAW} = r_a P_{\rm rf}/l_{\rm IDT} = 1.5$ W/m. Using the numerical model described in Ref. 2, we determined the threshold amplitude of the longitudinal piezoelectric field for acoustic transport to be $F_x^{(min)} = 1.8$ kV/cm. From the latter, we estimate an effective transport mobility $\mu_{\rm eff} = v_{\rm SAW}/F_x^{(min)} = 220$ cm$^2$/(Vs).

For acoustic powers above the threshold, the transfer efficiency reaches a maximum and then decreases for higher powers. High acoustic powers lead to a reduction of the radiative recombination probability over the whole NW. The reduction in $r_t$ is not due to a reduction of the transport efficiency, but rather attributed to the fact that at high rf-powers recombination is more efficiently suppressed at the remote site than in the illumination area. This occurs because the latter is continuously populated by carriers generated by the laser beam.

### C. Simulations of acoustic transport in nanowires

The simulations of the acoustic transport in the NW were carried out by solving the one-dimensional drift/diffusion equations for the electron ($n$) and hole ($p$) concentrations under the influence of the SAW field. In order to simulate the excitonic PL maps, the exciton concentration $N$ must also be obtained simultaneously to $n$ and $p$. The model used in this paper is a simplified version of that presented in Ref. 3. In particular, we assumed that the photoexcited carrier density is sufficiently low to make screening effects negligible. Under these conditions, the drift-diffusion equations for $n$ and $p$ take the form:[3]

$$\frac{\partial n}{\partial t} + \mu_n \frac{\partial}{\partial x}\left(n \frac{\partial \Phi}{\partial x}\right) - \mu_n V_T \frac{\partial^2 n}{\partial x^2} = G - c\, np \quad , \tag{S2a}$$

$$\frac{\partial p}{\partial t} - \mu_p \frac{\partial}{\partial x}\left(p \frac{\partial \Phi}{\partial x}\right) - \mu_p V_T \frac{\partial^2 p}{\partial x^2} = G - c\, np \quad , \tag{S2b}$$

where $\mu_n$ and $\mu_p$ are the electron and hole mobilities, and $V_T$ is the thermal voltage. The rate $G(x,t)$ of photogeneration of electron-hole pairs in the NW is taken to mimic the spatial and temporal profile of the laser light impinging on the sample. The term $c\,np$ is used to represent the rate at which electron-hole pairs are annihilated to form excitons in the ground state, and $c$ is the corresponding exciton formation coefficient. The transport is driven by the potential $\Phi(x,t)$ which, in the simulations presented here, has two contributions, $\Phi(x,t) = \Phi_{\mathrm{SAW}}(x,t) + \Phi_d(x)$. $\Phi_{\mathrm{SAW}}(x,t)$ is the SAW piezoelectric potential along the NW axis and has the form given by Eq. 1 of the main text. In order to simulate the trap at the remote recombination position $x_r = 4$ $\mu$m, we have incorporated a potential well $\Phi_d(x)$ able to capture both electrons and holes.

As discussed at length in Ref. 3, the various regimes of the acoustically induced charge transport are governed by the dimensionless parameter $\tilde{v}_{n,p} = 2\pi|\Phi_{\mathrm{SAW0}}|\mu_{n,p}/(\lambda_{\mathrm{SAW}} v_{\mathrm{SAW}})$, where $\Phi_{\mathrm{SAW0}}$ and $v_{\mathrm{SAW}}$ are the piezoelectric potential amplitude and wave velocity, respectively. $\tilde{v}_{n,p}$ is the ratio between the maximum velocity for electrons and holes in the potential and the SAW velocity.

The spatiotemporal dynamics of the exciton concentration $N(x,t)$ is given by the equation:

$$\frac{\partial N}{\partial t} - D_X \frac{\partial^2 N}{\partial x^2} = c\, np - \frac{N}{\tau_X} \quad . \tag{S3}$$

where $D_X$ is the exciton diffusion constant and $\tau_X$ is the exciton lifetime for radiative

recombination. In this paper, the measured PL intensities are compared with the calculated exciton recombination rate given by $I_{\rm PL}(x,t) = N(x,t)/\tau_X$.

The details of the numerical procedure for solving the system of differential equations given by Eqs. S2 and S3 are described in Ref. 3. The numerical simulations require, among other parameters, the SAW potential amplitude as well as carrier mobilities. For definiteness we have taken the typical values $\Phi_{\rm SAW0} = 0.11$ V, $\mu_n = 10000$ and $\mu_p = 1000$ cm$^2$/Vs, yielding the dimensionless parameters $\tilde{v}_n = 17$ and $\tilde{v}_p = 1.7$, which results in efficient acoustic transport for both types of carriers. The size and depth of the trap potential $\Phi_d$ at $x_r = 4$ $\mu$m was assumed to be sufficiently large to prevent carrier extraction by the SAW field. We note that the model can be easily modified to address other situations.

Figure S3a reproduces the time-resolved PL profiles at $x_r$ of Fig. 3g of the main text. These profiles are compared with the simulations performed under the mentioned conditions

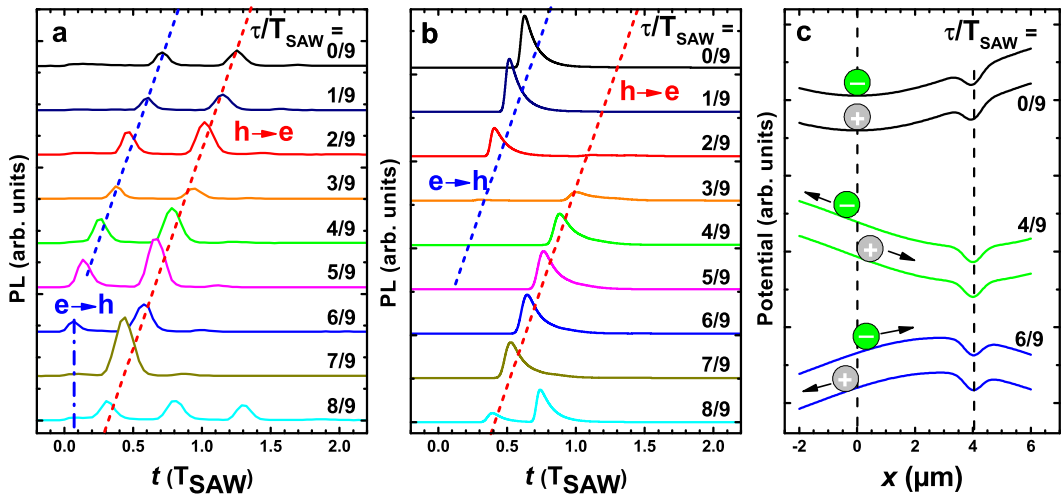


FIG. S3. **Time-evolution of the remote photoluminescence (PL). a**, Measured and **b,** calculated profiles for the remote PL in an intrinsic NW obtained by integrating the PL intensity around the remote trapping (and recombination) centers close to $x_r$ (indicated by the dotted line in Fig. 3a–f of the main text) for different surface acoustic wave (SAW) phase delays $\tau/T_{\rm SAW}$ (cf. Eq. 1 of the main text). **c,** Profiles for the piezoelectric potential $\Phi_{\rm SAW}(x, t = 0)$ used in the simulations, for selected SAW phases. The nanowire extends from $x = -2$ $\mu$m to $x = 6$ $\mu$m and the carriers are generated by a short laser pulse at $x = 0$. The local minimum at $x_r = 4$ $\mu$m models the remote trap and recombination center. Pulses $h \to e$ ($e \to h$) in **a** and **b** denote recombination events where transported holes (electrons) recombine with electrons (holes) trapped close to $x_r$.

for intrinsically undoped NWs (Fig. S3b). Both sets of curves show a good agreement except for two important differences. For $\tau/T_{SAW} < 3/9$ the experimental curves show a second remote PL pulse in Fig. S3a that does not appear in the simulations. The origin of this peak is attributed to the partial detrapping of holes from the traps and their subsequent return to $x_r$ half a SAW cycle latter, when they recombine with trapped electrons. These second pulses do not appear in the simulations since the deep trapping potential prevents carrier detrapping and forces all carriers to recombine for $t < T_{SAW}$.

In the experiments, PL pulses are also observed at short times $t < 0.4\ T_{\rm SAW}$ (dot-dashed lines in Fig. S3a). This pulses could not be reproduced by simulations of intrinsic NWs carried out for different values of carrier mobilities and amplitudes of the SAW field. They can, however, be reproduced if the traps are assumed to be populated prior to the arrival of the laser pulses. We discuss here the differences in the simulation results between initial population by holes and electrons, which are displayed in the simulated profiles of Figs. S4a

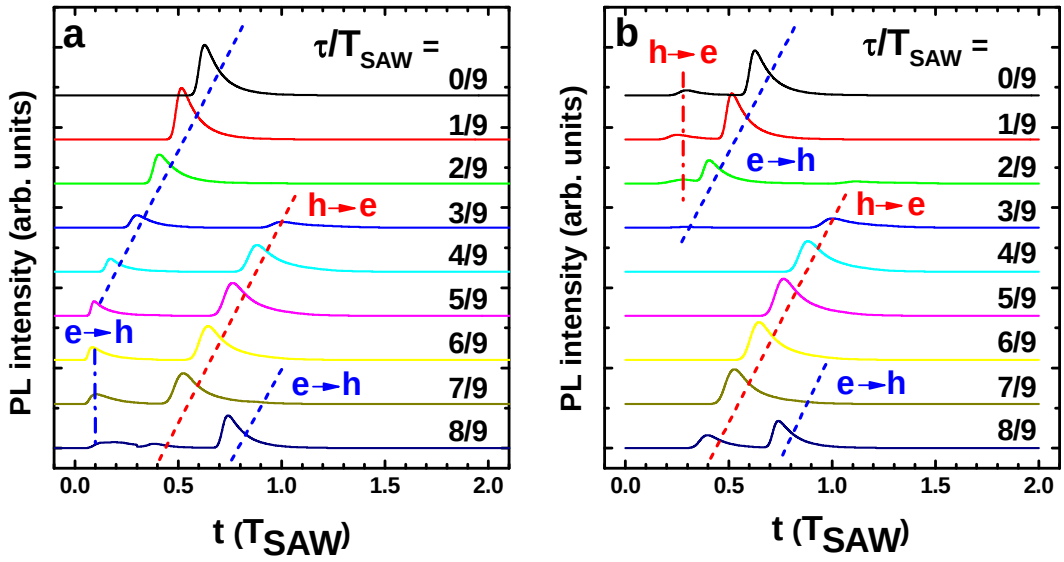


FIG. S4. **Simulation of the time evolution of the remote PL** calculated assuming that the remote trap at $x_r$ is initially populated by **a**, holes or **b**, electrons, for different phases $\tau/T_{\rm SAW}$ of the piezoelectric potential at the arrival time of the laser pulses ($t = 0$). The shapes of the profiles at $t = 0$ are shown in Fig. S3. Pulses $h \to e$ ($e \to h$) denote recombination events where transported holes (electrons) recombine with electrons (holes) trapped close to $x_r$. The initial population of the remote traps by electrons or holes leads to different delays for the pulses indicated by the dash-dotted lines.

and S4b, respectively. The overall shape of the PL profiles is very similar in these two cases with the main difference being the pulses at short times indicated by the dot-dashed vertical lines. Note that these pulses arrive at earlier times for initial hole population. The arrival time of these pulses is dictated by the transfer of one type of carriers (electrons or holes) from the illumination area to the populated trap. Due to the higher electron mobility, the transfer is faster when electrons are transferred to a hole-filled trap than when holes need to be transferred. An initial population of the traps with holes leads, therefore, to a better agreement with the experimental dynamics displayed in Fig. S3a. An initial hole population is also consistent with the fact that nominally undoped GaAs layers grown under similar conditions were observed to be p-type. The holes, therefore, probably arise from the ionization of acceptor centers in the NW.

## D. Photon-antibunching in GaAs/(In,Ga)As nanowires

### *1. Dependence of the transfer efficiency on acoustic power*

As described in the main text, the (In,Ga)As NWs (sample B) display a series of narrow spectral lines for wavelengths exceeding 840 nm, which are not observed in the pure GaAs NWs (sample A). Figure S5a displays a PL map of sample B within a narrow spectral region (compared to the one in Fig. 4 of the main text). The spectrum was recorded for excitation on the GaAs segment in the absence of a SAW. Remote PL emisson from the (In,Ga)As segment under these conditions is due to the diffusion of photoexcited carriers generated in the GaAs segment. When a SAW is applied, the (In,Ga)As PL initially increases (Figs. S5b-d) due to the acoustic charge transport to the (In,Ga)As segment. Note, in particular, that the line at 870 nm becomes the strongest one under remote excitation. This behavior, together with the fact that it is spectrally separated from other centers, justifies its choice for the photon-autocorrelation measurements in Fig. 5. For high rf-powers ($>$ 10 dBm, Figs. S5e-f), the strong piezoelectric fields reduce radiative recombination probability, leading to the quenching of the PL signal. In this power range, one also observed the broadening of the emission lines induced by the modulation of their energy levels by the SAW field.

As stated in the main text, Fig. S5 also shows weak lines within the GaAs segment with the same energy as the (In,Ga)As emission lines. The latter have been attributed

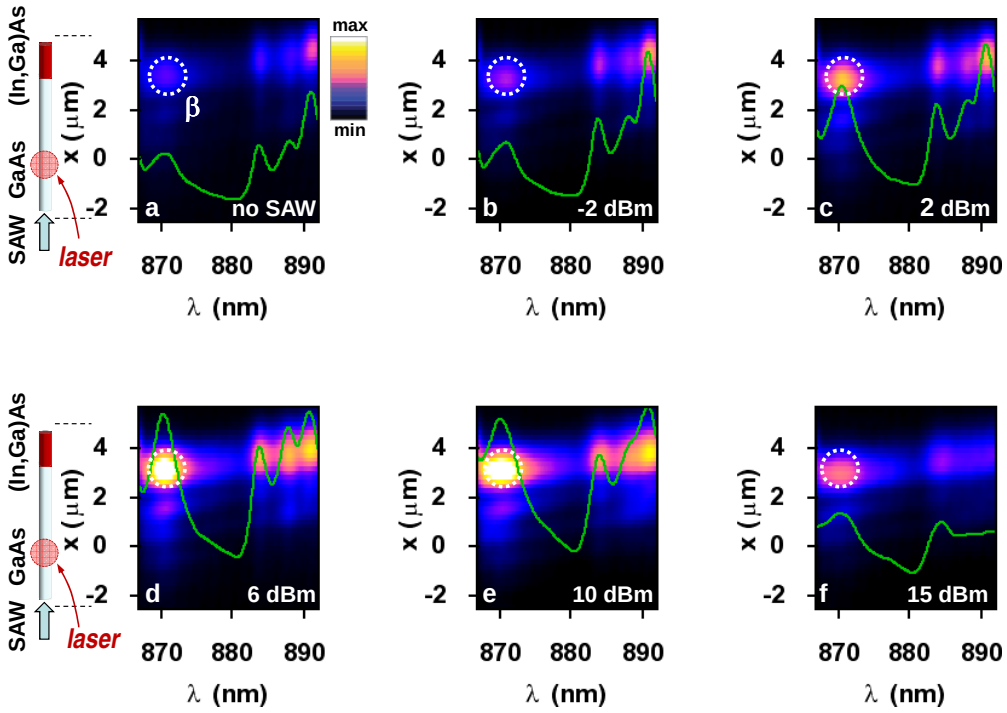


FIG. S5. **Dependence of the PL on SAW power.** The PL images (same color scale for all images) were recorded for different SAW powers by illuminating the GaAs segment with a focused laser spot (see diagrams on the left side). The dashed cycle marked $\beta$ shows the emission line probed in the autocorrelation measurements of Fig. 5c. The solid curves show PL spectra obtained by integrating the emission from the (In,Ga)As segment. Note that the spectra shape of the emission in the GaAs segment follows closely the one in the (In,Ga)As segment.

to the guiding of the emission from the (In,Ga)As segment through the GaAs one, which is transparent in this wavelength region. Note that when the acoustic power is changed, the intensity and spectral width of these lines follow closely the ones irradiating from the (In,Ga)As segment. In particular, their intensity increase at moderate rf powers, in contrast with the behavior for the GaAs-related lines observed at shorter wavelengths ($< 840$ nm, cf. Fig. 4).

In a second set of experiments to address the nature of the lines on the GaAs segment, we have recorded PL maps by directly exciting the (In,Ga)As segment using a focused laser beam (not shown). The measurements were carried out without applying a SAW. Due to the small dimensions of the NW, carriers may also be created in the GaAs segment. By performing experiments with different light excitation powers, we verified that the spectral

shape of the narrow lines on the GaAs segment again follows the one detected on the (In,Ga)As segment. These results are, therefore, also consistent with light guiding. Messing *et al.*[4] have recently reported on the formation of a thin (In,Ga)As layer on the GaAs sidewalls during the growth of the (In,Ga)As sections on GaAs NWs. A similar process may also occur during the growth of sample B. However, it is unlikely that a thin (In,Ga)As layer on the GaAs segment will have the same emission energy as in the (In,Ga)As segment.

### *2. Photon autocorrelation measurements*

For the photon correlation experiments on sample B, we have selected the lines at 870, 890, and 930 nm (cf. Fig. 4), which have (i) the highest emission intensity under acoustic excitation and (ii) the strongest dependence on acoustic power. From these lines, only the one at 870 nm (indicated by the dashed circle marked as $\beta$ in Fig. 4 and S5, which corresponds to the collection region for the autocorrelation measurements of Fig. 5c) showed a measurable anti-bunching in the range of acoustic powers studied. This center is also spectrally isolated from the others, thus making its selection easier using band pass filter.

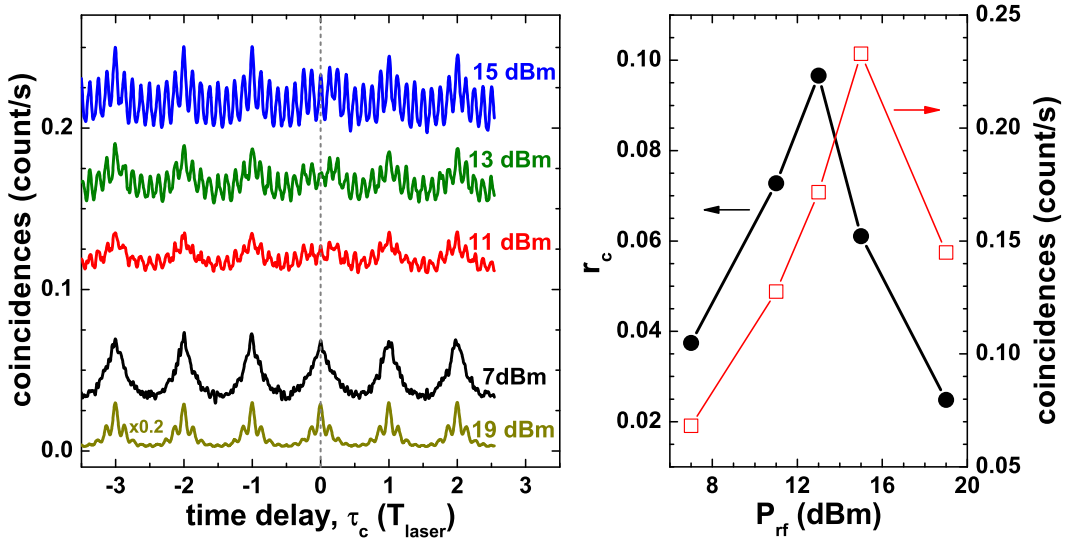


FIG. S6. **Dependence of the autocorrelation histograms on acoustic power. a**, Autocorrelation histograms recorded under the condition of Fig. 5c (configuration $\beta$) for different acoustic excitations using a fixed laser intensity. **b**, Comparison between the degree of antibunching $r_c$ and average coincidence rate.

In order to further corroborate the role of the acoustic transport for non-classical light emission, we show in Fig. S6 autocorrelation histograms for the 870 nm center under different acoustic powers. Both the coincidence rate (which depends on the transfer efficiency) and its suppression at $\tau_c = 0$ varies strongly with acoustic power. This behavior is quantified in Fig. S6b, which compares the average coincidence rate with the degree of antibunching $r_c$ defined in the main paper. Although the maxima for the two curves are slightly shifted, the high antibunching levels correlate well with a high transfer efficiency.

## REFERENCES


[1]K. Yamanouchi, C. H. S. Lee, K. Yamamoto, T. Meguro, and H. Odagawa, "GHz-range low-loss wide band filters using new floating electrode type unidirectional transducers," in IEEE Ultrason. Symp. (IEEE, New York, 1992) p. 139.

[2]M. M. de Lima, Jr. and P. V. Santos, "Modulation of photonic structures by surface acoustic waves," Rep. Prog. Phys. **68**, 1639 (2005).

[3]A. García-Cristóbal, A. Cantarero, F. Alsina, and P. V. Santos, "Spatiotemporal carrier dynamics in quantum wells under surface acoustic waves," Phys. Rev. B **69**, 205301 (2004).

[4]M. E. Messing, J. Wong-Leung, Z. Zanolli, H. J. Joyce, H. H. Tan, Q. Gao, L. R. Wallenberg, J. Johansson, and C. Jagadish, "Growth of straight inas-on-gaas nanowire heterostructures," Nano Letters **in print**, – (2011), http://pubs.acs.org/doi/pdf/10.1021/nl202051w.